Available online at www.sciencedirect.com
ScienceDirect
Journal of Power Sources 161 (2006) 413–419
JOURNAL OF POWER SOURCES
www.elsevier.com/locate/jpowsour

Anode barrier layers for tubular solid-oxide fuel cells with methane fuel streams

Huayang Zhu [a,*], Andrew M. Colclasure [a], Robert J. Kee [a], Yuanbo Lin [b], Scott A. Barnett [b]

[a] *Colorado School of Mines, Golden, CO 80401, USA*
[b] *Northwestern University, Evanston, IL 60208, USA*

Received 3 March 2006; received in revised form 13 April 2006; accepted 14 April 2006
Available online 8 June 2006

Abstract

Experimental results in button cells show that a porous chemically inert barrier layer can extend the range of coke-free operation on Ni–YSZ anode structures, even with pure methane as the fuel. The first objective of this paper is to assist interpreting these results using computational models that consider porous-media transport and heterogeneous reforming chemistry. The second objective is to predict the performance of a chemically inert barrier layer in a tubular, anode-supported, solid-oxide fuel cell.

Keywords: SOFC; Barrier layer; Reforming chemistry; Porous-media transport; Computational modeling; Tubular SOFC

1. Introduction

Solid-oxide-fuel-cell (SOFC) system performance can potentially be improved by introducing hydrocarbon fuels directly into the stack, without the need for upstream reforming processes. However, the propensity for coke formation on Ni-based anodes restricts hydrocarbon levels in the fuel stream. Using button-cell experiments, Barnett and coworkers have demonstrated that chemically inert or catalytically active barrier layers can enable the use of hydrocarbon fuels [1–4]. This paper develops and applies reactive-flow models to explore the efficacy of barrier layers in tubular SOFC systems.

The models incorporate fluid flow, porous-media transport and chemistry, and electrochemical charge transfer [5]. Methane-reforming chemistry on Ni is modeled with an elementary reaction mechanism [6]. Results of the models include gas-phase composition and current density along the length of the tube as well as gas-phase and surface-adsorbate composition through the thickness of the porous anode. Using methane as the fuel, the paper presents comparisons of systems with barrier and non-barrier membrane-electrode assemblies (MEA).

Chemically inert barrier layers are designed to isolate the Ni-based anode from direct contact with high hydrocarbon concentrations without the presence of sufficient reaction products (i.e., H_2O and CO_2) to inhibit coking. The barrier impedes the transport of electrochemically formed products from the three-phase region toward the fuel channel. It also impedes the transport of hydrocarbon fuel toward the dense-electrolyte interface. Thus, as a hydrocarbon encounters the Ni–YSZ, the steam (and CO_2) levels are sufficient to inhibit coking and facilitate steam reforming (and dry reforming). The barrier may have a different (usually lower) porosity than the Ni–YSZ. The button-cell experiments use a 700 micron Ni–YSZ anode layer and a 400 micron barrier layer that is fabricated as a mixture of partially stabilized zirconia (PSZ) and ceria [1].

Given the excellent barrier-layer performance of a button cell operating on methane [1], the objective of this paper is to predict the performance in a relatively large tubular cell. The tubular cells modeled in this paper (illustrated in Fig. 1) use the same MEA structure as in the button-cell experiments. After developing a physical model of the button-cell MEA, the model is then incorporated into a larger model that represents the tubular cell. In addition to coke inhibition, it is found that the barrier layer has the effect of producing a more uniform current-density profile, although at the cost of reducing local power density.

* Corresponding author. Tel.: +1 303 273 3890; fax: +1 303 273 3602.
E-mail address: hzhu@mines.edu (H. Zhu).

0378-7753/$ – see front matter © 2006 Elsevier B.V. All rights reserved.
doi:10.1016/j.jpowsour.2006.04.101

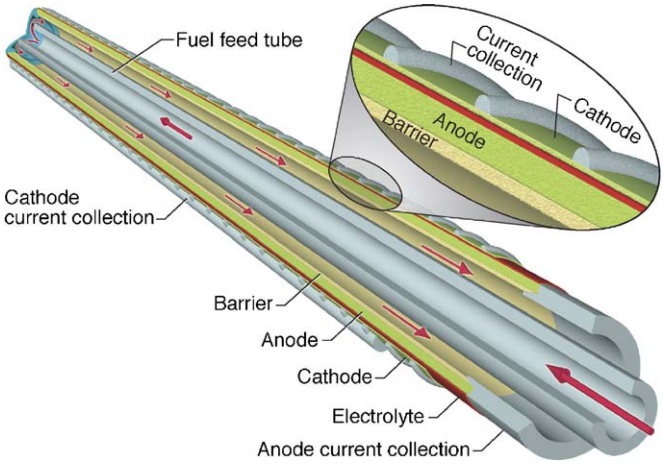

Fig. 1. Illustration of an anode-supported tubular fuel cell with a barrier layer.

2. Button-cell experiments

Lin et al. [1] have developed button-cell experiments to demonstrate and characterize the significant benefits of barrier layers in extending coke-free operating conditions with methane-fueled SOFCs. Using physical models [5] that are calibrated to represent the button-cell experiments, the experimental results can be projected into systems-level applications. This paper focuses on tubular cells.

Fig. 2 reproduces polarization measurements for button cells with and without a barrier as reported by Lin et al. [1]. The two cells were fabricated to be identical except for the barrier layer. Each cell has a 700 μm thick Ni–YSZ anode, a 20 μm thick dense yttria-stabilized zirconia (YSZ) electrolyte, and a 50 μm thick porous LSCF ($La_{0.6}Sr_{0.4}Co_{0.8}Fe_{0.2}O_3$) cathode, using a gadolinium-doped ceria (GDC) interface layer. The 400 μm thick porous barrier layer is composed of partially stabilized zirconia (PSZ) and ceria, which are both coke-resistant. In both cases the fuel is humidified methane (3% H_2O) and the oxidizer is air.

At sufficiently high current densities, the cells can operate stably and coke-free even without a barrier. At sufficiently low current densities both cells suffer performance degradation as a result of coke formation. However, the barrier results in coke-free operation at significantly lower current densities, enabling stable operation for practical ranges of operating conditions.

As shown in Fig. 2 the cell without a barrier layer has a higher power density. However, because of carbon deposition the non-barrier cell cannot operate stably with methane as the fuel at low current densities (i.e., below 1.8 A cm^{-2}). In fact, a special procedure is needed to measure the polarization characteristics. When operating at high current density (low cell potential) there is sufficient electrochemically generated steam available to suppress coking. Measurements at low current density are more complex. Beginning with stable operation at high current density, the cell potential is rapidly switched to a higher voltage. After a few seconds, a new low-current-density operating condition is established. Simulations, using the model described subsequently, show that the time scale for establishing a new steady condition is under one second. The cell is held in the

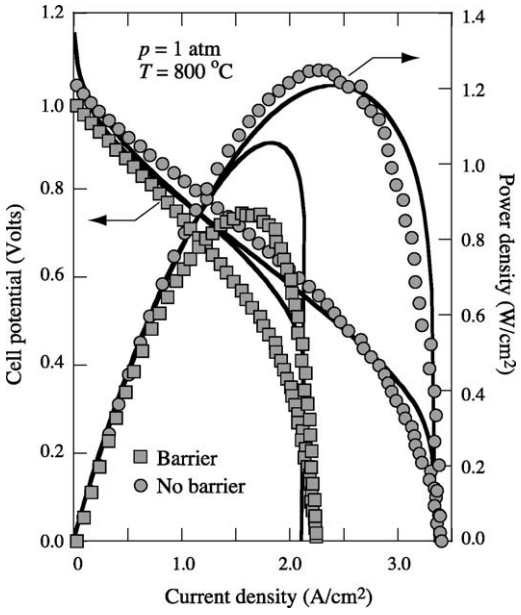

Fig. 2. Comparison of model and measurements for button cell running on a humidified (3% H_2O) methane. The data marked with circles does not have a barrier layer and the data shown with squares is taken with a barrier layer.

low-current condition long enough to make a measurement, then switched again to high current to suppress the coking. Because carbon deposition is a relatively slow process, this procedure is suitable for generating polarization characteristics, such as in Fig. 2.

The measured polarization curves (Fig. 2) show differences between the button-cell performance with and without a barrier. Generally speaking, the observed behavior is qualitatively as expected. However, some of the differences are not anticipated. The open-circuit potentials and specific resistances at low current density are expected to be about the same for both cells. This is because at low current the concentration overpotential should be negligible in either case. At high current density, the barrier contributes significant transport resistance. Thus it is expected that the barrier case should have a higher specific resistance and a lower limiting current density.

The observed difference in open-circuit potential is difficult to explain, since at open circuit (i.e., no current flow) the cell potential should be unaffected by the barrier. For all current densities, the data for the barrier cell indicate higher specific resistance than the data for the non-barrier cell. At low current density, where the transport resistance is low, this is an unanticipated result. At high current density, where the barrier contributes significantly to transport resistance, the barrier cell shows higher resistance as expected. Also, as expected, the barrier cell has a considerably lower limiting current density. Some of the unanticipated differences may be attributed to the fact that the two cells were fabricated separately and are probably not identical in all respects.

Using the model described in Zhu, et al. [5], parameters were fit to represent the measured performance of the button cells. Results of the MEA model are shown in Fig. 2 as solid lines. The physical parameters in the model, which are listed in Table 1, are adjusted to develop a good fit to the measured data. Detailed

Table 1
Parameters for modeling the MEA structure

Parameters	Value (units)
Anode	
Thickness (L_a)	700 (μm)
Porosity (ϕ)	0.35
Tortuosity (τ)	4.80
Pore radius (r_p)	0.20 (μm)
Particle diameter (d_p)	1.00 (μm)
Specific catalyst area (A_s)	1080 (cm^{-1})
Exchange current factor ($i^*_{H_2}$)	8.5 ($A\,cm^{-2}$)
Anodic symmetry factor (α_a)	1.5
Cathodic symmetry factor (α_c)	0.5
Cathode	
Thickness (L_c)	50 (μm)
Porosity (ϕ)	0.35
Tortuosity (τ)	4.00
Pore radius (r_p)	0.25 (μm)
Particle diameter (d_p)	1.25 (μm)
Exchange current factor ($i^*_{O_2}$)	2.4 ($A\,cm^{-2}$)
Anodic symmetry factor (α_a)	1.5
Cathodic symmetry factor (α_c)	0.5
Electrolyte: $\sigma_{el} = \sigma_0 T^{-1} \exp(-E_{el}/RT)$	
Thickness (L_{el})	20 (μm)
Activation energy (E_{el})	8.0E4 ($J\,mol^{-1}$)
Ion conductive pre-factor (σ_0)	3.6E5 ($S\,K\,cm^{-1}$)
Barrier:	
Thickness (L_{el})	400 (μm)
Porosity (ϕ)	0.175
Tortuosity (τ)	6.00
Pore radius (r_p)	0.15 (μm)
Particle diameter (d_p)	0.8 (μm)

definitions of the parameters and the theory concerning how they enter the model are found in Zhu, et al. [5].

3. Tubular cell

Fig. 1 illustrates the anode-supported tubular geometry that is used in subsequent analysis. This is a single-ended design, where gas manifolding and current collection are handled at one end of a closed tube. The fuel enters the cell through an inner feed tube, with a return flow in the annular space formed between the outside of the feed tube and the anode structure. The dense electrolyte and cathode are applied to the outside of the tube. In the subsequent analysis, we assume that undiluted air is available everywhere on the outside of the tube. In this tubular configuration, cathode current collection is accomplished by wrapping wires around the outer diameter. Anode current collection is accomplished by axial conduction through the Ni–YSZ. Sammes and coworkers have recently published information concerning the fabrication of tubular anode-supported cells [7,8].

Although the models are capable of representing voltage variations along the tube length, we do not use that capability here. In this paper we assume a uniform cell potential. In other words, we assume that there are no axial voltage drops in the anode or cathode. In practice, of course, there are voltage losses that must be accommodated. However, the objective of this paper is not to present a design for a particular cell. Rather, it is to discuss the potential viability and performance benefits of barrier layers. The practical considerations for current collection are design-dependent and do not substantially affect the discussion of barrier layers.

Another practical consideration is a start-up procedure. The barrier concept only works when there is sufficient electrochemically generated H_2O and CO_2 to prevent coking. Thus there could be carbon formation during start-up transients. One approach for start-up is to bleed air into the fuel stream. By doing so, cell heating can be accomplished in a catalytic partial oxidation (CPOX) mode. When sufficient oxygen is available, carbon formation can be suppressed [9]. Once the cell has achieved operating temperature, the air feed can be terminated.

4. Physical model

The physical model used here is a relatively minor extension of the model reported by Zhu, et al. [5]. Thus, only a brief summary is presented here, noting modifications and differences.

Gas flow in the annular space between feed tube and the anode is treated as plug-flow, neglecting radial spatial variations [10]. Gas-phase chemistry is neglected owing to very small reaction rates for methane at temperatures below around 900 °C [11]. Reactive porous-media transport is modeled using a Dusty-Gas Model (DGM), which represents pressure-driven convective fluid flow as well as ordinary and Knudsen molecular diffusion [12]. In the tubular setting the porous-media problem is represented in cylindrical coordinates, and axial transport is neglected. Fig. 3 illustrates some of the physical processes in global form. Reforming chemistry within the Ni–YSZ anode is modeled with an elementary reaction mechanism that incorpo-

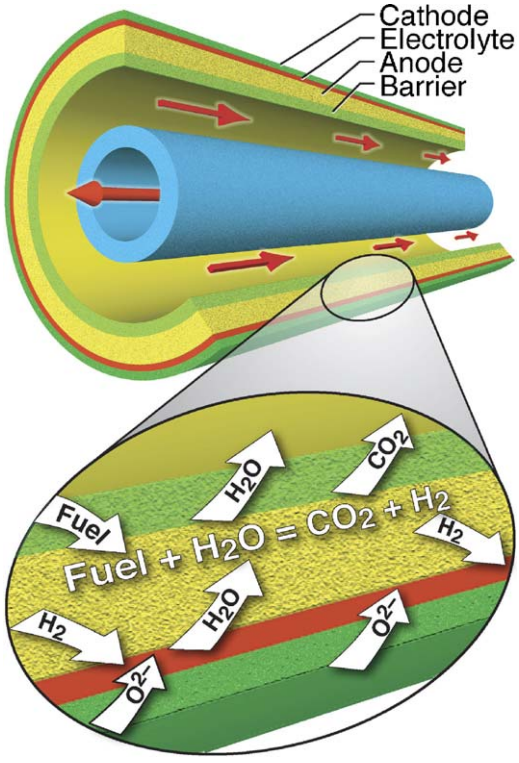

Fig. 3. Global charge-transfer and reforming processes within a tubular anode-supported SOFC.

rates steam and dry reforming as well as partial oxidation [6]. This mechanism considers 42 reactions among six gas-phase species and 12 surface-adsorbed species. The mechanism does not specifically account for coke-formation reactions. Within the barrier layer, which is considered to be chemically inert, there is porous-media transport but no chemistry. Charge transfer is assumed to proceed at the interface between the anode structure and the dense electrolyte. The available three-phase area is taken as an empirical parameter (incorporated in the exchange current density i_o^*) that is adjusted to represent the button-cell performance. The model assumes that charge transfer proceeds only through H_2, which is produced as a result of reforming chemistry [13,5]. Although CO is available, we assume that the charge-transfer via CO is slow compared to H_2 and that CO is easily converted to H_2 and CO_2 via water–gas-shift processes.

5. Model predictions

For the sake of illustration and discussion of barriers, we choose specific tube geometries and operating conditions. The anode-supported tubes are 60 cm long, with an inside diameter of 1.08 cm for the non-barrier case. The 400 μm barrier is applied to the inside of the 700 μm Ni–YSZ anode. Thus, the inside diameter of the barrier is 1.0 cm. In both cases the electrolyte-layer diameter is $D_{el} = 1.22$ cm, which maintains the same electrochemically active three-phase region for both cases. The inner feed tube has an outside diameter of 0.6 cm for the non-barrier case, but is slightly smaller for the barrier case so as to maintain the same annular-flow cross-sectional area for the barrier and non-barrier cases. The annular gap available for gas flow is approximately 0.2 cm. In all cases the fuel composition is 97% CH_4 and 3% H_2O, and the inlet velocity is 30 cm s^{-1}. The cathode is exposed to undiluted air everywhere on the outside of the tube. The operating voltage is held uniform at 0.75 V and the temperature is assumed to be isothermal at 800 °C. The operating conditions are set to achieve nearly complete fuel utilization in the 60 cm tube length.

Figs. 4 and 5 show model predictions for the non-barrier and barrier cases, respectively. In both figures the upper panel shows gas-phase mole fractions in the annular space and local current density as functions of the axial position. Note that the current density is referenced to the electrolyte area, at a diameter of 1.22 cm. The drop-down panels show gas-phase mole fractions within the pore spaces through the thickness of the anode structure. In the barrier case, the dashed line shows the interface between the barrier and the chemically active porous anode.

Consider first the non-barrier case (Fig. 4). Keep in mind that the non-barrier case is not practically viable because of coking associated with methane contacting Ni in the upstream portions of the tube. Nevertheless, the non-barrier case provides a point of comparison for the barrier case. As methane enters the tube, it is rapidly reformed to H_2 and CO. There are local maxima in the H_2 and CO mole fractions around 3 cm into the tube. This behavior is caused by the fact that reforming consumes CH_4 faster than the resulting H_2 can be consumed electrochemically. The left-hand drop-down panel ($x = 0$ cm) provides further evidence of this behavior. Local maxima of H_2 and CO are seen within the anode structure. The gradients toward the three-phase boundary (bottom of the graph) are caused by electrochemical consumption of H_2 and water-gas-shift conversion of CO to CO_2. There are also gradients of CO and H_2 toward the annular channel, indicating mass fluxes of these species into the flow channel. By 10 cm along the channel, the net H_2 and CO fluxes are from the channel toward the anode three-phase region at the dense-electrolyte interface. At this point, there are strong net fluxes of reaction products H_2O and CO_2 through the anode structure toward the channel. Consequently the levels of H_2O and CO_2 in the channel increase, while the fuel species H_2, CH_4, and CO decrease. The current density also decreases along the tube length as the fuels are depleted and diluted in products. The flow

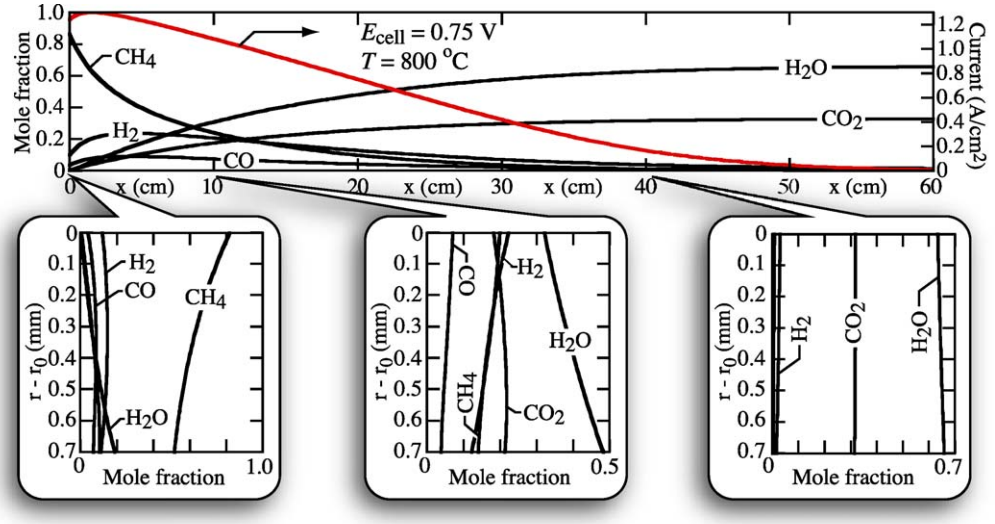

Fig. 4. Solution profiles for the non-barrier case. The upper panel shows the gas-phase composition in the annular flow space and the local current density as a function of axial position in the tube. The drop-down panels show gas-phase composition in the pore spaces of the Ni–YSZ anode structure at three axial positions along the tube. The top of the drop-down graphs is at the channel interface and the bottom is at the dense-electrolyte interface. The variable $r_0 = 0.54$ cm is the inner radius of the anode structure.

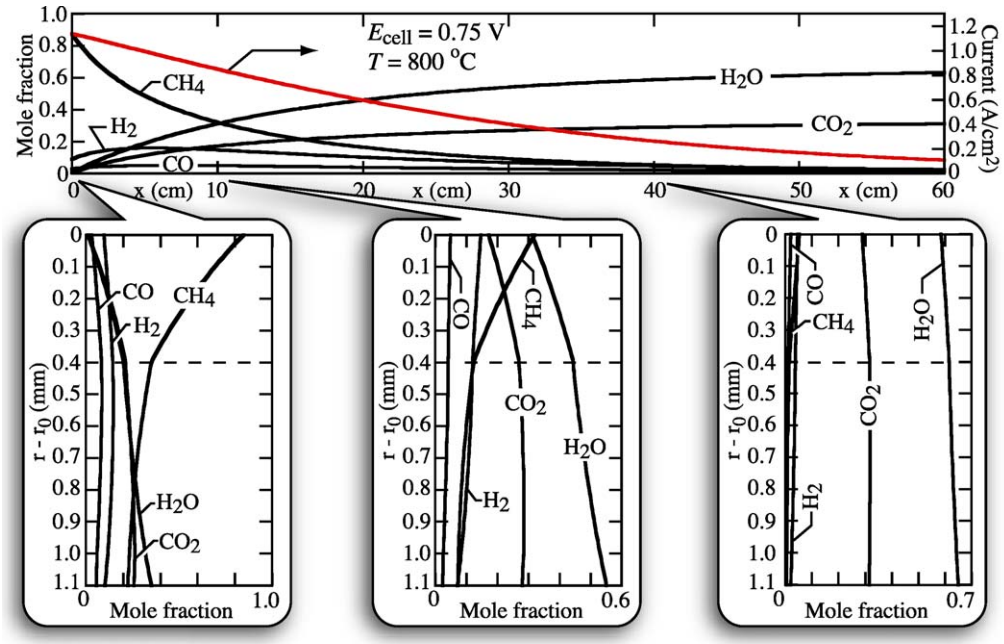

Fig. 5. Solution profiles for the barrier case. The upper panel shows the gas-phase composition in the annular flow space and the local current density as a function of axial position in the tube. The drop-down panels show gas-phase composition in the pore spaces of the anode structure at three axial positions along the tube. The dashed line show the interface between the barrier and the Ni–YSZ. The variable $r_0 = 0.5$ cm is the inner radius of the anode structure.

rates were set to achieve nearly complete fuel utilization. So by a length of 60 cm, the current density has nearly vanished and the gas flow is composed of only products H_2O and CO_2.

In the entry regions of the tube, there are high methane concentrations in contact with the Ni. Because of coking (or other carbon-deposit formation) this situation is highly problematic. In fact, operating such a cell with pure hydrocarbon fuels is impractical. Indeed, this provides the motivation for the barrier concept.

Fig. 5 shows predicted performance for the barrier case. Although there are some differences, the gas composition in the annular space and the local current density behave qualitatively similarly to the non-barrier case. The most important benefits of the barrier are associated with the CH_4 concentrations that are in contact with Ni. The drop-down panels reveal sharp changes in species gradients at the barrier interface with the Ni–YSZ structure. The high CH_4 concentrations in the chemically inert barrier do not cause deposit formation. Because the barrier impedes the flux of CH_4 into the anode and the flux of H_2O and CO_2 out, the CH_4 only contacts Ni where there are sufficient levels of H_2O and CO_2 available to suppress carbon formation.

Although not entirely definitive, chemical equilibrium provides a practical indicator for coking propensity. Following the general approach by Sasaki and Teraoka [14], Fig. 6 is a C–H–O ternary plot that shows regions of equilibrium solid-phase carbon as functions of the elemental composition of a mixture. The equilibrium states are computed by a free-energy minimization algorithm using the CHEMKIN software. Above the line marked 800 °C there is solid carbon (graphite) in equilibrium. Below the line, only gas-phase species are present at equilibrium. The circular markers show the elemental compositions as functions of axial position in the tube for the barrier and non-barrier cases. It is evident in the non-barrier case that equilibrium predicts solid carbon for the first 6–8 cm in the tube. In the downstream sections, there is sufficient steam (and other oxygenated species) available to suppress the carbon formation. In these examples, the barrier has been specifically designed so that the elemental composition at the barrier-anode interface (dashed line in Fig. 5) is always below the equilibrium solid-carbon line. Thus, it is expected that the barrier tube would not suffer a coke problem, which is consistent with experimental observations in the button cell [1]. It may be noted that the barrier need not extend the entire length of the tube. At some axial location there is sufficient steam and carbon dioxide in the flow channel that the barrier is no longer needed. It should also be noted that these results are simulated for a cell voltage of 0.75 V. A lower cell voltage or different operating temperature may require different barrier characteristics for stable operation.

Fig. 7 compares some results that are derived from the solutions shown in Figs. 4 and 5. The electrical efficiency, utilization, and power are all functions of the axial position in the tube. The efficiency is defined as

$$\varepsilon(x) = \frac{P_e(x)}{Q_{in}} = \frac{\pi D_{el} \int_0^x i(x) E_{cell} dx}{\dot{m}_{f,in} \Delta h_{f,in}}, \quad (1)$$

where P_e is the electrical power produced (Watts) and Q_{in} is the heating value associated with completely oxidizing the fuel stream to CO_2 and H_2O. The operating cell potential is E_{cell}, the diameter of the electrolyte is D_{el}, and the local current density (based on electrolyte area) is $i(x)$. Thus the integral in the numerator represents the net electrical power as a function of tube axial position. The heating value is determined as the product of the fuel mass-flow rate and the heat of reaction associated with the global oxidation reaction, Δh. Fuel utilization is de-

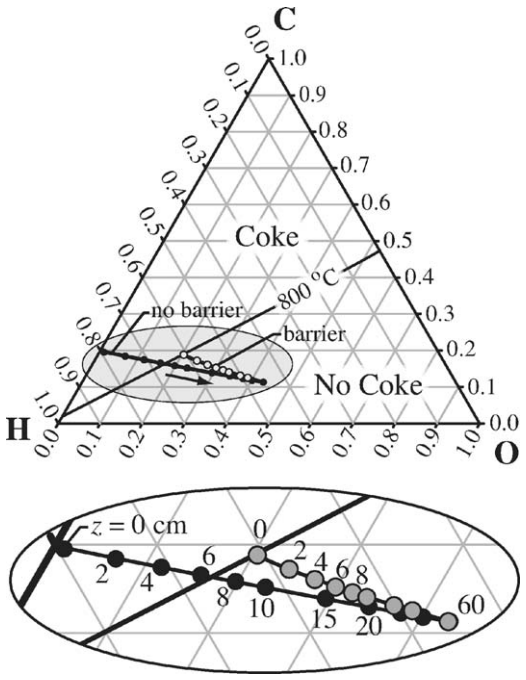

Fig. 6. Ternary equilibrium diagram showing regions where solid carbon (graphite) is present. The black markers show the elemental composition in the annular flow channel as a function of axial position for the non-barrier case (i.e., conditions of Fig. 4). The light markers show the elemental composition within the Ni–YSZ anode at the interface with the barrier layer as a function of axial position for the barrier case (i.e., conditions of Fig. 5). In both cases, the equilibrium is evaluated at the position where coke-formation is most likely.

fined in terms of the heating value of the inlet stream and the local heating value of the fuels within the tube,

$$U(x) = 1 - \frac{\dot{m}_{\mathrm{f},x}\Delta h_{\mathrm{f},x}}{\dot{m}_{\mathrm{f,in}}\Delta h_{\mathrm{f,in}}}, \tag{2}$$

where the "in" refers to the inlet flow and x is the axial position along the tube. Within the tube the available fuels are considered to be CH_4, H_2, and CO.

The net power for these tubes is around 80–90 W. Fig. 7 shows that the power density is lower in the barrier case than in the non-barrier case. In other words, for the specified operating conditions, the barrier tube needs to be longer than the

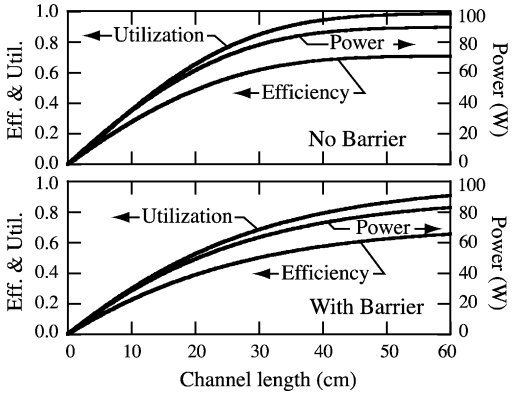

Fig. 7. Profiles of efficiency, utilization, and net power as functions of axial position in the tubes. The upper panel shows the profiles for the non-barrier case (i.e., Fig. 4) and the lower panel shows results for the barrier case (i.e., Fig. 5).

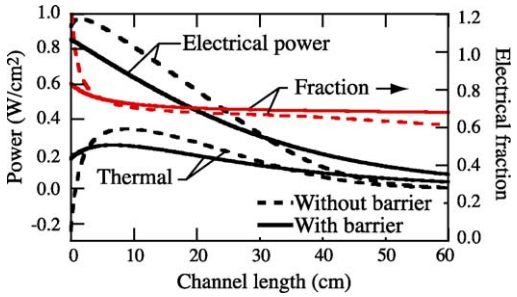

Fig. 8. Electrical power density, thermal power density, and electrical fraction as functions of axial tube position. The dashed lines show the non-barrier case and the solid lines show the barrier case.

non-barrier tube to achieve the same net power and conversion efficiency. Nevertheless, the predicted performance for the two tubes is comparable. The efficiencies are in the range of 60–70% at utilization levels of around 90%. This is very good performance using a pure hydrocarbon fuel. Of course, it must be kept in mind that the non-barrier tube would not be practical owing to deposit formation.

Interestingly, despite somewhat lower power density, there are aspects of the barrier cell that are superior to the non-barrier cell (in addition to avoiding coking). Fig. 8 shows electrical power (i.e., numerator of Eq. (1)) and thermal power as functions of axial position. As discussed in Zhu, et al. [5] the local thermal power is the result of heating associated with reforming chemistry, ion-transport resistance, and charge-transfer inefficiencies. The curves marked "fraction" in Fig. 8 show the fraction of net power (i.e., electrical plus thermal) that is electrical.

In the non-barrier case, there is a strong endotherm associated with high steam-reforming rates near the tube entrance. In fact, the thermal power is predicted to be negative in the vicinity of the tube entrance. This means that external heat would be needed to maintain the cell temperature. In the barrier case, this endotherm is significantly moderated, because the barrier impedes the species fluxes to the Ni catalyst where reforming proceeds. The result is much more uniform heating rates along the length of the tube, which eases the task of maintaining uniform temperatures along the tube length.

It should be noted that it would be impractical to draw 80 W from these tubes using axial current collection through the anode layer. The axial voltage drop would be much too large. As a practical matter, some design for low-resistance anode current collection would be needed. For example, the tube could be segmented with multiple current taps along the length. Further, a net anode-plus-barrier wall thickness of only 1.1 mm may be too thin for structural reasons in a long tube. There are certainly viable approaches to thickening or strengthening the tube walls, while retaining the beneficial characteristics of a barrier. In any case, the objective of this paper is to illustrate the characteristics and benefits of barrier layers, not to design a specific tube cell.

6. Conclusions

With chemically inert anode-side barrier layers, SOFC button cells can be operated stably and coke-free using hydrocarbon fuels. Motivated by the demonstrated success of the button-cell

experiments [1], we have extended and applied physical models to predict performance in relatively large tubular cells with barrier layers. The results show that barrier layers can be designed to develop SOFC systems that are capable of operating coke-free on hydrocarbons, with all reforming accomplished internally. The paper uses a particular tubular system to illustrate essential features of the barrier approach.

Acknowledgments

We gratefully acknowledge many insightful discussions with Dr. Grover Coors (CoorsTek, Inc.) concerning the fabrication and performance of tubular cells. The CSM work was supported by the Office of Naval Research through a Research Tools Consortium under grant number N00014-05-1-0339. The Northwestern contribution is based upon work supported by the Department of Energy, National Technology Laboratory, under award number DE-FC26-05NT42625.

References

[1] Y. Lin, Z. Zhan, S. Barnett, Improving the stability of direct-methane solid oxide fuel cells using anode barrier layers, J. Power Sources 158 (2006) 1313–1316.
[2] Z. Zhan, Y. Lin, S. Barnett, Anode catalyst layers for direct hydrocarbon and internal reforming SOFCs, SOFC IX 9 (2005) 1321–1330.
[3] Y. Lin, Z. Zhan, J. Liu, S. Barnett, Direct operation of solid oxide fuel cells with methane fuel, Solid State Ionics 176 (2005) 1827–1835.
[4] Z. Zhan, S. Barnett, Use of a catalyst layer for propane partial oxidation in solid oxide fuel cells, Solid State Ionics 176 (2005) 871–879.
[5] H. Zhu, R. Kee, V. Janardhanan, O. Deutschmann, D. Goodwin, Modeling elementary heterogeneous chemistry and electrochemistry in solid-oxide fuel cells, J. Electrochem. Soc. 152 (2005) A2427–A2440.
[6] E. Hecht, G. Gupta, H. Zhu, A. Dean, R. Kee, L. Maier, O. Deutschmann, Methane reforming kinetics within a Ni–YSZ SOFC anode, Appl. Catal. A 295 (2005) 40–51.
[7] N. Sammes, Y. Du, R. Bove, Design and fabrication of a 100 W anode-supported micro-tubular SOFC stack, J. Power Sources 145 (2005) 428–434.
[8] Y. Du, N. Sammes, Fabrication and properties of anode-supported tubular solid oxide fuel cells, J. Power Sources 136 (2004) 66–71.
[9] Z. Zhan, J. Liu, S. Barnett, Operation of anode-supported solid oxide fuel cells on propane-air fuel mixtures, Appl. Catal. A 262 (2004) 255–259.
[10] R. Kee, M. Coltrin, P. Glarborg, Chemically Reacting Flow: Theory and Practice, John Wiley, 2003.
[11] G. Gupta, E. Hecht, H. Zhu, A. Dean, R. Kee, Gas-phase reactions of methane and natural gas with air and steam in non-catalytic regions of a solid-oxide fuel cell, J. Power Sources 156 (2006) 434–447.
[12] E. Mason, A. Malinauskas, Gas Transport in Porous Media: the Dusty-Gas Model, American Elsevier, New York, 1983.
[13] R. Kee, H. Zhu, D. Goodwin, Solid-oxide fuel cells with hydrocarbon fuels, Proc. Combust. Inst. 30 (2004) 2379–2404.
[14] K. Sasaki, Y. Teraoka, Equilibria in fuel-cell gases: II. the C—H—O ternary diagrams, J. Electrochem. Soc. 150 (2003) A885–A888.